CHEMISTRY OF MATERIALS
Cite This: Chem. Mater. 2018, 30, 4720−4727
Article
pubs.acs.org/cm

Site-Specific Doping of Mn^{2+} in a CdS-Based Molecular Cluster

Fumitoshi Kato and Kevin R. Kittilstved*

Department of Chemistry, University of Massachusetts Amherst, 374 Lederle GRT, 710 North Pleasant Street, Amherst, Massachusetts 01003, United States

Supporting Information

ABSTRACT: The synthesis and characterization of a CdS-based molecular cluster, $[Cd_{10}S_4(SPh)_{16}]^{4-}$ (Cd_{10}), with site-specific substitution of Cd^{2+} with Mn^{2+} impurities are reported. The formation of the Cd_{10} cluster from the smaller $[Cd_4(SPh)_{10}]^{2-}$ (Cd_4) cluster involves a metastable intermediate cluster, $[Cd_8S(SPh)_{16}]^{2-}$ (Cd_8), that is detected by electrospray ionization mass spectrometry (ESI-MS). To account for this unexpected intermediate, we propose a complex equilibrium between Cd_4, Cd_8, and Cd_{10} exists that we exploit to introduce Mn^{2+} impurities at both core and surface cation sites of the Cd_{10} lattice. We demonstrate through two synthetic procedures that differ only in the sequence in which Mn^{2+} is introduced to the reaction dictates its speciation in the cluster. Introducing dopants at an early stage of the synthesis prevents full conversion of Cd_8 to Cd_{10}; however, it yields core doped Cd_{10} clusters. Addition of Mn^{2+} ions after the preparation of Cd_{10} yields only surface doped clusters. The composition of the doped clusters is systematically characterized by ESI-MS and exhibits speciation-dependent peak intensities. Photoluminescence (PL) spectra of the Mn^{2+}-centered $^4T_1 \rightarrow {}^6A_1$ transition also exhibits significant differences in peak position and PL lifetimes that are consistent with the expected variation in ligand field strength experienced by these two metal sites. However, ESI-MS and PL collected on "aged" samples indicate slow displacement of Mn^{2+} from core sites. This study provides new insights to the growth mechanism of clusters that remained rather elusive and demonstrates how the cluster surface dynamics and cluster equilibria can be exploited for precise doping of these well-defined semiconductor analogues.

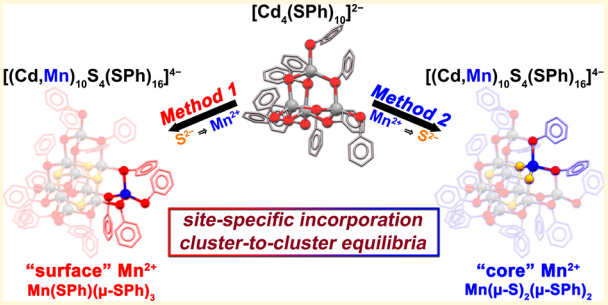

INTRODUCTION

The chemical and physical properties of small, discrete molecular and magic-sized clusters have received great attention in recent years due to their inherent monodispersity in contrast to their colloidal nanocrystal analogues.[1,2] Similar to quantum confined nanocrystals, these semiconductor nanoclusters also exhibit size-dependent electronic structures.[3−10] Interest in the synthesis of colloidal nanocrystals with better-defined composition and narrow size distributions has led many to focus their studies on the chemistry of molecular clusters that may serve as precursor clusters in the synthesis of nanocrystals.[1,11−17] Some of these molecular clusters have also been employed as single-source precursors for the synthesis of pure and doped colloidal semiconductor nanocrystals.[6,18,19]

The substitutional doping of paramagnetic transition metal ions in these clusters produces large magneto-optical effects and dopant-related photoluminescence (PL) reminiscent of diluted magnetic semiconductor quantum dots (DMS-QDs).[20−23] Recent examples involving Mn^{2+} as the impurity ion in semiconductor nanoclusters includes $(Zn_{1-x}Mn_xTe)_{13}$, which exhibited long-lived emission from the Mn^{2+} dopant,[24] and $(Cd_{1-x-y}Zn_xMn_ySe)_{13}$ that exhibits well-resolved giant Zeeman splittings of the HOMO−LUMO (excitonic-like) transition.[25,26] Despite the monodispersity of these doped nanoclusters, little is known regarding the chemical stability and distribution of impurities in such small clusters where even a single dopant can surpass the solid solubility limit in the bulk semiconductor. Even these small tridecameric magic-sized clusters must possess more than one unique site in the lattice that expands the difficulty in correlating material properties with dopant speciation.

The class of metal chalcogenide nanoclusters employed in this study adopt "supertetrahedral" molecular structures with potentially multiple unique crystallographic sites.[1,14,15,24−31] The molecular clusters utilized herein are based on anionic cadmium thiophenolate clusters with NMe_4^+ counterions and also S^{2-} ions at the cores of the larger clusters.[29,32−35] Of particular importance to this study include the following: $[Cd_4(SPh)_{10}]^{2-}$, Cd_4; $[Cd_8S(SPh)_{16}]^{2-}$, Cd_8; $[Cd_{10}S_4(SPh)_{16}]^{4-}$, Cd_{10}; and $[Cd_{17}S_4(SPh)_{28}]^{2-}$, Cd_{17}. The Cd_4 cluster has one unique cation site that is coordinated to $4PhS^-$ ligands (three μ-PhS^- and one monovalent PhS^-) and defines the surface site that is conserved in every Cd_n cluster in this study. Scheme 1 shows both the similarities Cd-site as well as crystallographic differences between the Cd_8 and Cd_{10} clusters. Specifically, in addition to the 4 equiv surface sites, Cd_8 and Cd_{10} contain additional "core" sites. The remaining 4

Received: April 10, 2018
Revised: June 13, 2018
Published: June 13, 2018

DOI: 10.1021/acs.chemmater.8b01482
Chem. Mater. 2018, 30, 4720−4727

Scheme 1. Comparison of Cd_4, Cd_8, and Cd_{10} Structures[32,34,38]

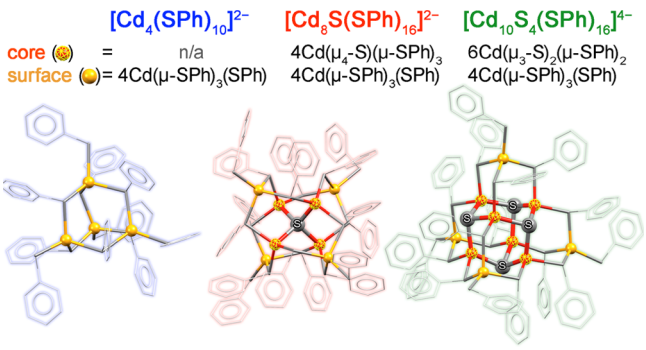

and 6 Cd^{2+} ions, respectively, occupy the core cation sites of the lattice defined by Cd^{2+} in a pseudotetrahedral arrangement with both μ-PhS^- and μ-S^{2-} ligands. The Cd_{17} cluster possesses 4 surface, 12 core, and one additional central site with a $Cd(\mu_4\text{-}S)_4$ unit at its center. Studies aimed at resolving the mechanism of cation exchange in molecular or magic-sized clusters have been relatively limited.

We recently reported the incorporation of Co^{2+} ions into preformed Cd_4, Cd_{10}, and Cd_{17} molecular clusters.[36,37] We determined a positive correlation exists between the metal-ion exchange kinetics of substitutional Co^{2+} impurities and the interconversion rate of the surface PhS^- ligands bound to the Cd^{2+} ions at each vertex (see Scheme 1 for Cd_{10}). The ligand interconversion rate was found to decrease significantly with increasing cluster size as evidenced by variable-temperature ^1H NMR spectroscopy and provides strong evidence for the importance of fast surface dynamics in facilitating fast metal-ion exchange. However, despite this finding, the main limitation of low-temperature doping of preformed Cd_n clusters from metal ions in solution is that substitution occurs only at the surface sites and typically not with core sites. Sufficient understanding of the reaction mechanism governing heteronuclear cluster formation is thus required to develop an effective site-specific doping strategy.

Herein, we present two room-temperature syntheses of Mn-doped Cd_{10} cluster, $(NMe_4)_4[Cd_{10-x}Mn_xS_4(SPh)_{16}]$ ($Mn{:}Cd_{10}$). The two syntheses differ only in the order in which the dopant and S^{2-} are added and also present an alternate method to prepare Cd_{10}. The two methods are referred to as method 1 ($Mn{:}Cd_{10}$-1) and method 2 ($Mn{:}Cd_{10}$-2), where Mn^{2+} and S^{2-} ions are added in different sequences to premade Cd_4 clusters. $Mn{:}Cd_{10}$-1 is similar to our previous study of $Co{:}Cd_{10}$, where the dopants were added to the premade Cd_{10} cluster.[36] The formation of Cd_{10} and $Mn{:}Cd_{10}$ was confirmed by ESI-MS, an analytical technique that has been proven to be a very effective tool to characterize the size, composition, structural evolution, and stability of various inorganic molecular clusters[28,39−44] and noble-metal clusters.[45−47] Spectroscopic and analytical characterization of the resulting $Mn{:}Cd_{10}$ clusters display features consistent with Mn^{2+} ions substituted primarily at surface sites in $Mn{:}Cd_{10}$-1 or core sites in $Mn{:}Cd_{10}$-2. However, the substitution of Mn^{2+} at core Cd sites in $Mn{:}Cd_{10}$-2 is found to be unstable with slow exchange of dopant ions to either surface sites or diffusion out of the cluster. Systematic titration studies reveal that the conversion of Cd_4 to Cd_{10} appears to include a metastable Cd_8 intermediate that we hypothesize is responsible for Mn^{2+} incorporation at core sites in the Cd_{10} cluster via method 2. The site-specific doping of substitutional Mn^{2+} ions in the Cd_{10} clusters prepared from these two methods provides intriguing possibilities for extending this strategy of utilizing metastable doped clusters to synthesize larger nanoclusters, including magic-sized clusters and even diluted magnetic semiconductor quantum dots with homogeneous dopant distributions.

EXPERIMENTAL SECTION

Chemicals. Cadmium nitrate tetrahydrate ($Cd(NO_3)_2{\cdot}4H_2O$, 99.999%, Alfa Aesar), sodium sulfide nonahydrate ($Na_2S{\cdot}9H_2O$, 98%, Acros Organics), thiophenol (PhSH, 99%, ACROS Organics), manganese nitrate hydrate ($Mn(NO_3)_2{\cdot}xH_2O$, 99.98%, Alfa Aesar), tetramethylammonium hydroxide (TMAOH, 99%, Fisher Chemical), anhydrous acetonitrile (CH_3CN, 99.8%, ACROS Organic), anhydrous methanol (CH_3OH, 99.8%, ACROS Organics), and triethylamine (Et_3N, 99%, Fisher) were used without further purification. Caution! Thiophenol is extremely toxic and has an unpleasant odor. Handle with caution according to the material safety data sheet. All manipulations were handled under inert atmosphere of dry N_2 using the glovebox.

Synthesis of Cd_{10}. The typical synthesis of Cd_{10} involves direct addition of elemental S to Cd_4, where PhS^- ligands reduce S to S^{2-} to yield Cd_{10}.[35] We did not use this literature method. Instead, we employed the following procedure originally reported[29] to prepare Cd_{17} that was modified to prepare Cd_{10}. By decreasing the amount of Cd^{2+} added, it is possible to synthesize Cd_{10}.

Briefly, a solution of PhS^- was prepared by adding PhSH (0.53 mL, 5.20 mmol) and Et_3N (0.73 mL, 5.20 mmol) to 4.0 mL of CH_3CN in a single-neck RB flask with magnetic stirring. A solution of $Cd(NO_3)_2{\cdot}4H_2O$ (0.660 g, 2.14 mmol) in CH_3CN (2.2 mL) was then added to PhS^- to yield a white precipitate. A 0.24 M stock solution of $Na_2S{\cdot}9H_2O$ (0.288 g, 1.2 mmol) dissolved in CH_3OH (5.0 mL) was added, resulting in dissolution of the white precipitate followed by the emergence of turbid light-yellow solution. A solution of 0.234 M TMAOH (0.212 g, 1.17 mmol) in CH_3OH (5.0 mL) was then added to the solution and left undisturbed for 3 days. The lightly yellowish powder was then filtered and washed with methanol.

Synthesis of Mn-Doped Cd_{10} by Method 1. Similar to the synthesis of Cd_{10}, however, the $Mn(NO_3)_2{\cdot}xH_2O$ (0.537 g, 2.14 mmol) dissolved in methanol (1 mL) was added to the reaction solution before the TMAOH solution. The pale yellowish orange product was left undisturbed for 5 days, vacuum filtered, and washed with methanol.

Synthesis of Mn-Doped Cd_{10} by Method 2. After the addition of $Cd(NO_3)_2$ to a solution of PhS^-, 0.5 mL of the 5.0 mL Na_2S stock solution was added, which dissolved the white precipitant and yields clear yellow solution. $Mn(NO_3)_2{\cdot}xH_2O$ (0.537 g, 2.14 mmol) in 1.0 mL methanol was then added to the solution followed by successive addition of the remaining Na_2S and TMAOH solutions. The pale reddish powder was left undisturbed for 5 days, vacuum filtered, and washed with methanol.

Physical Characterization. Room temperature absorption, photoluminescence, and excitation spectra of the clusters in N_2-purged CH_3CN solutions were collected with either a Cary 50 or a Cary Eclipse spectrophotometer. The optical density of the absorption spectra was <0.6 over throughout the UV and visible regions. High-resolution electrospray ionization mass spectra (ESI-MS) were collected in negative ion mode with a Bruker MicroTOF-II. The concentration of analyte solution was kept at ∼30 μM, and the flow rate of samples was set to 3 μL/min for ESI-MS. Analysis of the mass spectra was performed using the mMass program.[48]

RESULTS AND DISCUSSION

Alternative Synthesis of the Cd_{10} Cluster. Figure 1 shows the negative-ion mode ESI-MS collected at −20 V in a narrow region of m/z values for samples taken at various steps during the synthesis of Cd_{10} (see Supporting Information for

DOI: 10.1021/acs.chemmater.8b01482
Chem. Mater. 2018, 30, 4720−4727

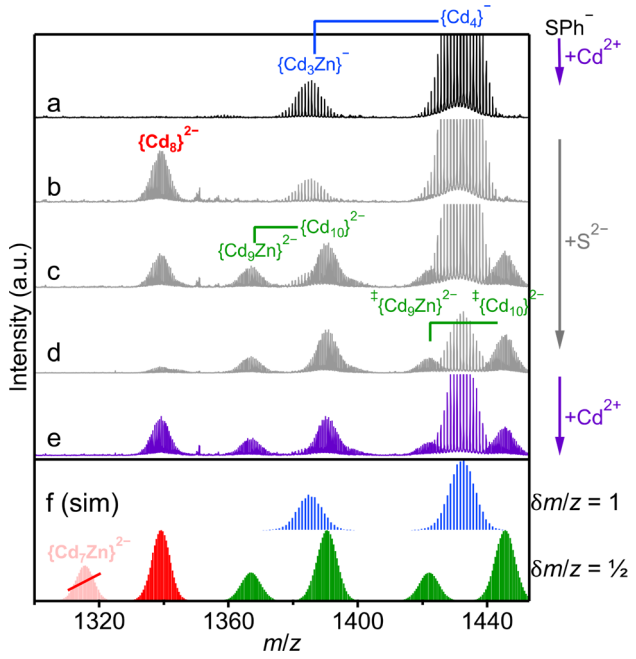

Figure 1. Negative-ion mode ESI-MS over an expanded set of aliquots taken during the sequential titration of Na_2S and $Cd(NO_3)_2$ reactants to a Cd_4 solution (see Supporting Information for full spectra). All spectra were collected at a cone voltage of −20 V. Mass spectra were collected after sequential addition of the following to a solution containing 5.20 mmol of PhS^-: (a) 2.14 mmol of $Cd(NO_3)_2$, (b) 0.240 mmol of Na_2S, (c) 0.720 mmol of Na_2S, (d) 1.20 mmol of Na_2S, and (e, purple) 0.405 mmol of $Cd(NO_3)_2$. (f, Sim) Peak simulations for $[Cd_4(SPh)_9]^-$ $\{Cd_4\}^-$ (blue), $[Cd_8S(SPh)_{16}]^{2-}$ $\{Cd_8\}^{2-}$ (red), $[Cd_{10}S_4(SPh)_{14}]^{2-}$ $\{Cd_{10}\}^{2-}$ (green), and $[Cd_{10}S_4(SPh)_{14}]^{2-}$ + PhSH $\{^{\ddagger}Cd_{10}\}^{2-}$ (green), respectively. Note the offset between singly and doubly charged fragments ($\delta m/z$ = 1 and $^1/_2$, respectively). The aliquots removed from the reaction solution used in this figure were turbid with the exception for sample b. Before injection into the ESI-MS instrument, all samples were dissolved in additional CH_3CN.

full spectra). After addition of ∼0.4 eq of Cd^{2+} to a solution of PhS^-, the formation of anionic Cd_4-related clusters is confirmed by the appearance of a major peak at m/z 1432 corresponding to the $[Cd_4(SPh)_9]^-$ fragment (Figure 1a). In addition, we also observe the Zn^{2+} exchange product, $[Cd_3Zn(SPh)_9]^-$, in the mass spectra that we attribute to Zn^{2+} contamination either from the mass spectrometer or the PhSH precursor (see Figure S4).[49]

Titration of Na_2S to the Cd_4 solution results in a significant decrease in the relative intensity of "Cd_4"-related fragments and the formation of intact Cd_8 clusters at m/z 1339 as shown in Figure 1b. Note the absence of Zn-exchanged Cd_8 clusters in the mass spectrum (see simulated spectrum in Figure 1f). Additional titration of Na_2S shown in Figures 1c and d results in further reduction of both Cd_4-related and Cd_8 fragments and the appearance of new features at m/z 1390 and 1445. These new fragments are attributed to Cd_{10} clusters with specific compositions of free and PhSH-bound $[Cd_{10}S_4(SPh)_{14}]^{2-}$ fragments, respectively. The Zn-contaminated Cd_{10} products are also observed. After complete addition of S^{2-} to the reaction solution, most of the Cd_4 and Cd_8 clusters have been converted to Cd_{10} clusters as shown in Figure 1d. Upon addition of the counterion, TMAOH, a light-yellow precipitate forms. After filtration and washing this powder, it was found to be primarily Cd_{10} by ESI-MS (see Figure S1). However, both Cd_4 and Cd_8 are detected in the initial supernatant (see Figure S2).

Further addition of Cd^{2+} to the turbid reaction solution yields more Cd_4-related fragments and Cd_8 clusters, as shown in Figure 1e. Further addition of $Cd(NO_3)_2$ after this step would yield Cd_{17} according to the literature protocol.[29] The reversibility in the relative concentrations of Cd_4 and Cd_{10} suggests an equilibrium exists between these clusters and includes Cd_8. The only other synthetic method to prepare Cd_{10} was reported by Dance and co-workers[35] and involves the addition of elemental sulfur to Cd_4 in the appropriate stoichiometry to afford Cd_{10} and the oxidation product of PhS^- that is Ph_2S_2. Dance and co-workers also reported that the reaction between Cd_{10} and Ph_2Se_2 in DMF yielded $[Cd_8S(SePh)_{16}]^{2-}$.[32] We propose two limiting scenarios, S-rich and Cd-rich, to explain the possible cluster equilibria involving Cd_4, Cd_8, and Cd_{10} species (see Scheme 2). Different

Scheme 2. Proposed Solution Equilibria of Cd_4, Cd_8, and Cd_{10} Clusters under S^{2-}-Rich and Cd^{2+}-Rich Conditions[a]

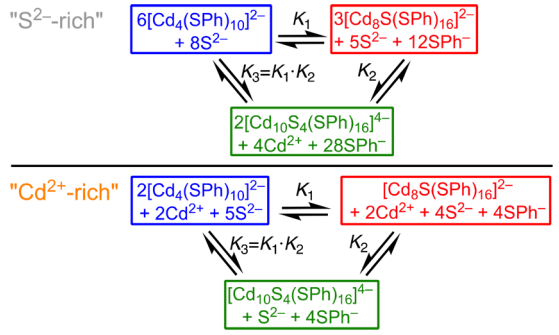

[a]The direction of the arrow closest to K_n represents the forward reaction.

assumptions were made for these mechanisms that are mainly associated with the chemical species present in the upper-left of each triangle scheme (designated in blue). The S-rich scheme is based on the assumption that all free Cd^{2+} ions are converted to Cd_4 when Cd^{2+} is added to the excess PhS^-. However, the Cd-rich scheme explicitly allows for free Cd^{2+} species and Cd_4 (and Cd_8) to be present in solution with S^{2-} (and PhS^-).

According to Scheme 2, if the formation of Cd_{10} during the titration reaction proceeds without total dissolution of the Cd_4 cluster, then it may be possible to utilize Mn^{2+}-doped Cd_4 clusters as the direct reactant to prepare either internally Mn^{2+}-doped Cd_8 clusters following K_1 or Mn^{2+}-doped Cd_{10} (K_3). However, if any of the clusters totally disassemble and then reassemble along any equilibrium pathway, then the kinetics should favor formation of undoped clusters. Thus, the likely speciation of Mn^{2+} ions in the latter scenario would only occur at surface sites of Cd_{10}. Both of these proposed mechanisms provide similar insight into the cluster conversion process that occurs during Cd_{10} synthesis and potentially enable metal ion exchange reactions to be targeted to specific cluster types.

Mn^{2+} Speciation in Cd_n Clusters. We performed two syntheses of Mn^{2+}-doped Cd_{10} clusters that differ only in the order in which $Mn(NO_3)_2$ is added. We refer to these as Mn:Cd_{10}-1, where Mn^{2+} was added after formation of Cd_{10}, and Mn:Cd_{10}-2, where Mn^{2+} was added after formation of Cd_4

DOI: 10.1021/acs.chemmater.8b01482
Chem. Mater. 2018, 30, 4720−4727

and Cd_8 (corresponds to the species shown in Figure 1b). For both Mn:Cd_{10} syntheses, the nominal Mn^{2+} concentration is equivalent to the total Cd^{2+} concentration (50 mol percent). Figure 2 shows the ESI mass spectra of the isolated and filtered

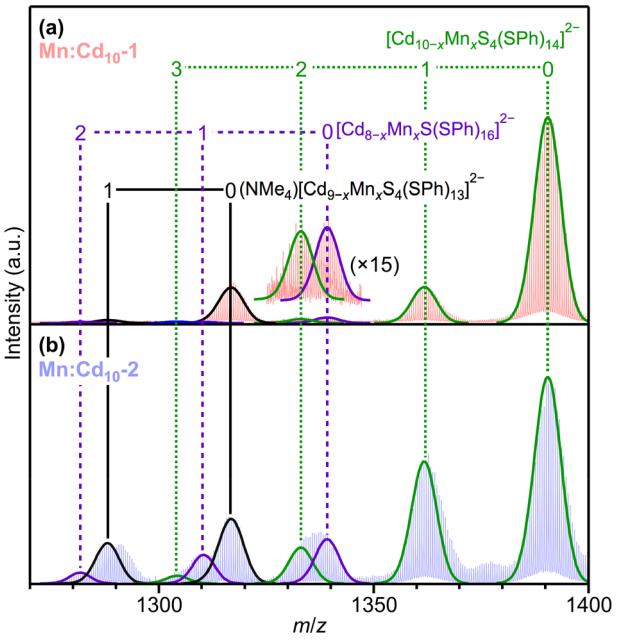

Figure 2. Negative-ion mode ESI mass spectra of (a) Mn:Cd_{10}-1 (M1) and (b) Mn:Cd_{10}-2 (M2) clusters in the region of the doubly ionized fragments ($\delta m/z = 0.5$): $[Cd_{10-x}Mn_xS_4(SPh)_{14}]^{2-}$ (blue), and $(NMe_4)[Cd_{9-x}Mn_xS_4(SPh)_{13}]^{2-}$ (black); and the Cd_8-derived cluster: $[Cd_{8-x}Mn_xS(SPh)_{16}]^{2-}$ (purple). All spectra were collected at a cone voltage of −20 V.

from both Mn:Cd_{10} syntheses where fragments with the general formula $[Cd_{10}S_4(SPh)_{14}]^{2-}$ (m/z 1390), $[Cd_8S(SPh)_{16}]^{2-}$ (m/z 1339), and $(NMe_4)[Cd_9S_4(SPh)_{13}]^{2-}$ (m/z 1317) are detected (see Figures S5 and S6 for full spectra). The major peak in Figure 2 for both Mn:Cd_{10} products is assigned to the Cd_{10} precursor cluster centered at m/z 1390. In addition, fragments containing up to three Mn^{2+} ions in the Cd_{10} fragments are detected with decreasing relative intensities at m/z values of 1362 (Cd_9Mn_1), 1333 (Cd_8Mn_2), and 1304 (Cd_7Mn_3), respectively. A very broad feature between m/z 1325 and 1350 clearly originates from two distinct fragments as shown on an expanded scale in Figure 2a. Deconvolution of this region reveals that the peaks match well to the simulated spectra of $[Cd_8S(SPh)_{16}]^{2-}$ centered at m/z 1339 and $[Cd_8Mn_2S_4(SPh)_{14}]^{2-}$ at m/z 1333. The final set of peaks originate from $(NMe_4)[Cd_{9-x}Mn_xS_4(SPh)_{13}]^{2-}$ product fragments at m/z 1317 (Cd_9Mn_0) and 1288(Cd_8Mn_1), respectively.

A clear difference between the two Mn:Cd_{10} products shown in Figure 2 is that the relative intensities of the doped fragments are always higher for the Mn:Cd_{10}-2 clusters where Mn^{2+} was added prior to Cd_{10} formation. In addition, there is much higher abundance of Cd_8 and Mn:Cd_8 clusters for Mn:Cd_{10}-2. The data in Figure 2 are summarized in Scheme 3. While it is tempting to attribute the increased relative abundance of Mn-doped Cd_{10} fragments to possible exchange of Mn^{2+} with Cd^{2+} ions in the Cd_{10} core, it is not supported by the ESI-MS data alone. Under low ionization conditions, the data shown in Figure 2 provide no direct information regarding

Scheme 3. Proposed Reaction for the Formation of Doped Cd_{10} Clusters

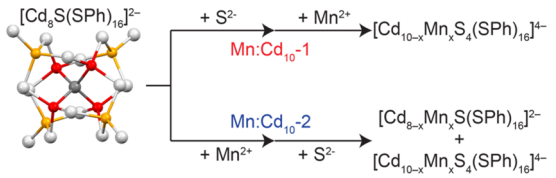

the Mn^{2+} speciation in the Cd_{10} cluster. In addition, the maximum number of Mn^{2+} ions in the Cd_{10} fragment by either synthesis is three, which could simply occupy just surface sites. This is the most likely scenario for Mn:Cd_{10}-1, where cation exchange between the preformed Cd_{10} and Mn^{2+} can occur only at the surface sites. However, although very small in relative peak intensity, Cd_8 and Mn-doped Cd_8 fragments were observed for Mn:Cd_{10}-1 in Figure 2a, suggesting reversibility of Cd_{10} to Cd_8 may occur by the addition of Mn^{2+} in a similar manner that Cd^{2+} addition caused destabilization of the Cd_{10} cluster shown in Figure 1e.

The mechanism for metal ion exchange in Cd_4 clusters most likely proceeds by association of metal ions to PhS^- ligands undergoing rapid interconversion with other bridging/surface PhS^- ligands in the cluster.[36,50] This requirement for exchange could be mediated by the presence of additional clusters in solution with faster ligand interconversion dynamics (i.e., less S^{2-} content) in solution.[36] Very slow metal ion exchange kinetics between intact clusters of similar[38] and dissimilar[39] clusters has been reported and may involve similar cluster equilibria.

For Mn:Cd_{10}-2, the synthesis involves adding Mn^{2+} after the initial formation of Cd_4 and Cd_8 clusters, but before the addition of the total amount of S^{2-} required to produce Cd_{10}. As shown in Figure 2b, there is also a considerable amount of fully intact Cd_8 clusters present that exchange up to 2 Mn^{2+} ions by ESI-MS (see red dashed lines in Figure 2b). This observation is consistent with an apparent positive correlation between the relative intensity of doped Cd_8 and Cd_{10} clusters with Mn:Cd_{10}-1 and Mn:Cd_{10}-2. Furthermore, this correlation would predict that Mn^{2+} and Cd^{2+} compete for S^{2-} coordination in solution that could lead to the incomplete conversion of Cd_8 to Cd_{10} under the high nominal Mn^{2+} mole percentages used here (50%).

It may seem reasonable to assume that the Cd_8 clusters prepared by the Mn:Cd_{10}-2 method were doped through surface metal ion exchange similar to Mn:Cd_{10}-1 and other Cd_n clusters. While very likely, both Mn^{2+} and Cd^{2+} ions can compete for available S^{2-} anions during cluster assembly with the Mn:Cd_{10}-2 method. This possible mechanism could allow at least some of the Mn^{2+} ions ligated to S^{2-} anions to be incorporated at Cd_8 core sites that may be retained when Cd_8 converts to Cd_{10}. Furthermore, the ESI mass spectra also suggest the dopant distribution is different between the two Mn:Cd_{10} clusters from the relative peak intensities shown in Figure 2. The relative intensities for all Mn^{2+}-doped clusters are significantly higher in Mn:Cd_{10}-2 than Mn:Cd_{10}-1.

We also examined the change in the relative intensities of the singly doped and nondoped Cd_{10} clusters as a function of increasing fragmentation via loss of up to two neutral $Cd(SPh)_2$ or $Mn(SPh)_2$ species (see Figure 3). The largest clusters are $[Cd_9Mn_1S_4(SPh)_{14}]^{2-}$ (Cd_9Mn_1 in the figure) and $[Cd_{10}S_4(SPh)_{14}]^{2-}$ (Cd_{10} in the figure) at m/z 1362 and 1390,

DOI: 10.1021/acs.chemmater.8b01482
Chem. Mater. 2018, 30, 4720−4727

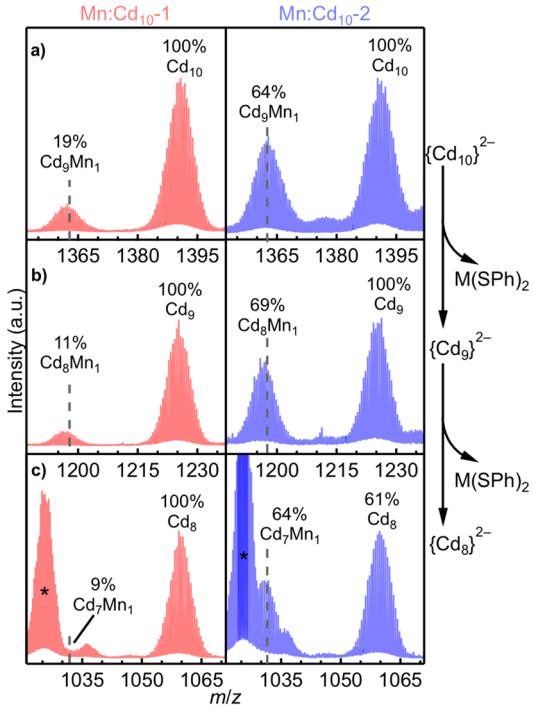

Figure 3. Negative-ion mode ESI mass spectra of Mn:Cd_{10}-1 (red, left panel) and Mn:Cd_{10}-2 (blue, right panel) in the region of the doubly ionized fragments ($\delta m/z$ = 0.5). The fragments in these focused regions correspond to (a) $[Cd_{10-x}Mn_xS_4(SPh)_{14}]^{2-}$, (b) $[Cd_{9-x}Mn_xS_4(SPh)_{12}]^{2-}$, and (c) $[Cd_{8-x}Mn_xS_4(SPh)_{10}]^{2-}$, where x = 0 and 1. The asterisk at m/z 1024 is $(NMe_4)[Cd_{10}S_4(SPh)_{16}]^{3-}$ ($\delta m/z$ = 0.33). The clusters were suspended in degassed CH_3CN and collected at a cone voltage of −40 V.

respectively. These fragments differ from the intact cluster by two PhS^- ligands that are removed by ionization. The most likely position for the cluster to lose the additional $M(SPh)_2$ fragments is also from these surface sites of the Cd_{10} cluster. The relative peak intensities of the Cd_9Mn_1 fragment in the Mn:Cd_{10}-1 clusters has ∼19% the intensity of the Cd_{10} fragment. This relative peak intensity steadily decreases with increasing removal of both $M(SPh)_2$ fragments, which is consistent with Mn^{2+} predominantly occupying surface sites. Contrary to Mn:Cd_{10}-1, the mass spectrum of Mn:Cd_{10}-2 does not exhibit this same trend. The relative peak intensity of the Cd_nMn_1 fragments remains fairly constant between 64 and 69% of the Cd_n fragments. The data presented in Figure 3 provides strong evidence that Mn^{2+} is located at core cation sites only in the Mn:Cd_{10}-2 clusters. However, without removing all surface cation sites with increasing stronger ionization voltage and confirming core Mn^{2+} substitution, we cannot determine the precise location of the dopants in Cd_{10} by ESI-MS.

Gated Photoluminescence Spectroscopy. We utilized photoluminescence (PL) spectroscopy to decipher whether the variation in the ligand fields between core and surface sites manifest themselves in the Mn^{2+}-centered PL spectra. The steady-state spectra of both Cd_{10} and Mn:Cd_{10} products is dominated by strong intraligand and metal-to-ligand charge transfer (MLCT) PL ranging from 305 to 345 nm (see Figure S9). The Mn:Cd_{10} PL is consistent with the ESI-MS data that confirm that the majority of Mn:Cd_{10} clusters do not contain Mn^{2+}. However, we were able detect the long-lived $^4T_1 \rightarrow {}^6A_1$ PL of pseudotetrahedral Mn^{2+} by collecting the PL after a delay of 100 μs after excitation to remove the fast Cd_{10} fluorescence. The resulting gated PL and PL excitation (PLE) spectra of the Mn:Cd_{10} clusters on normalized scales are shown in Figure 4. Both the energies and lifetimes of the

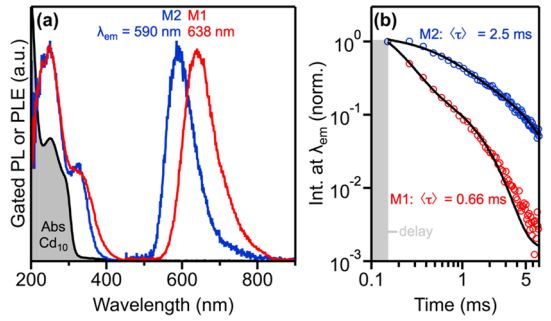

Figure 4. (a) Gated PL and PLE (left) spectra of Mn:Cd_{10}-1 (red) and Mn:Cd_{10}-2 (blue) samples in N_2-purged CH_3CN solutions. Spectra were collected within 5 min of preparation. The absorbance spectrum of Cd_{10} is also shown (black line with gray shading). (b) PL decay (dots) and biexponential fits (lines) of the Mn^{2+} PL from panel (a) on a logarithmic time scale. Average PL lifetimes, $\langle\tau\rangle$, were calculated using eq 2.

broad Mn^{2+}-centered PL are significantly different between the two clusters. The Mn:Cd_{10}-1 clusters display Mn^{2+} PL centered at 638 nm (1.94 eV), while the Mn:Cd_{10}-2 clusters display PL centered at 590 nm (2.10 eV).

The PL lifetimes of the Mn^{2+} PL display biexponential decay behavior that were fit using eq 1.[51]

$$I(t) = (\alpha_1/\tau_1)e^{-(t+t_0)/\tau_1} + (\alpha_2/\tau_2)e^{-(t+t_0)/\tau_2} \quad (1)$$

where α_1 and α_2 are the amplitudes, τ_1 and τ_2 are the PL lifetimes, and t_0 is the gate time of the measurement. We included the numerical results from the fits in Table S3. The average PL lifetimes were calculated by taking the weighted average of the individual PL lifetimes according to eq 2

$$\langle\tau\rangle = (\alpha_1\tau_1 + \alpha_2\tau_2)/(\alpha_1 + \alpha_2) \quad (2)$$

The average PL lifetime is found to be much shorter for Mn:Cd_{10}-1 ($\langle\tau\rangle$ = 0.66 ms) than Mn:Cd_{10}-2 ($\langle\tau\rangle$ = 2.5 ms). Both lifetimes are consistent with previously reported lifetimes for Mn^{2+}-doped in magic-sized clusters and QDs.[20,24,52]

The PLE spectra of Mn^{2+} PL exhibit energy transfer in the broad UV regions centered at 250 nm. This overlaps well with the absorption spectrum of Cd_{10} also shown in Figure 4. The UV absorption features is attributed to overlapping $\pi \rightarrow \pi^*$ intraligand transition of PhS^- and a ligand-to-metal charge transfer (LMCT) transition from PhS^- (HOMO) to Cd^{2+} 5s orbital (LUMO).[9,53] A shoulder centered at ∼325 nm is also observed in the PLE spectra of both Mn:Cd_{10} clusters that we attribute to a charge transfer transition involving the core: namely, S^{2-} 2p orbitals and Cd^{2+} 5s or Mn^{2+} 4s orbitals. Cd_{10} does not show any transition in this region, but a broad absorption ranging from ∼320 to 400 nm can be observed in concentrated solutions of Mn:Cd_{10} that we tentatively attribute to a Mn^{2+}-to-ligand charge-transfer transition (see Figure S8).

The difference in the energy of the $^4T_1 \rightarrow {}^6A_1$ PL is ∼160 meV between the two Mn:Cd_{10} clusters. The energy difference between the $^4T_1$ excited state and the $^6A_1$ ground state decreases with increasing ligand field strength.[54] The average ligand field imposed on the Mn^{2+} depends on whether it sits at a surface or core site in the Cd_{10} cluster. Evaluation of ligand

DOI: 10.1021/acs.chemmater.8b01482
Chem. Mater. 2018, 30, 4720−4727

field parameters for Mn^{2+} complexes is complicated by the lack of spin-allowed transitions; however, these parameters are known for Co^{2+} in two relevant clusters, $(PPh_4)_2[Co(SPh)_4]$ and $(NMe_4)_2[Co_4(SPh)_{10}]$, as well as CdS ($\mu_4$-$S^{2-}$).[55−57] The ligand-field parameters for Co^{2+} in the relevant lattices are given in Table 1. The ligand field strengths of both monovalent

Table 1. Experimental Ligand-Field Parameters for Tetrahedral Co^{2+} with PhS^- and S^{2-} Ligands[a]

lattice	10*Dq*	*B*	β[b]	ref
$[Co(SPh)_4]^{2-}$	−4030	619	0.63	55
$[Co_4(SPh)_{10}]^{2-}$	−4740	643	0.65	56
Co^{2+}:CdS	−3160	664	0.67	57

[a]All energies are in cm^{-1}. [b]Nephelauxetic ratio, β = *B*(complex)/*B*(free-ion). Free-ion value for Co^{2+} is 989 cm^{-1}.[58]

PhS^- and μ-PhS^- ligands are greater than μ_4-S^{2-}. Thus, Mn^{2+} coordination to PhS^- ligands is expected to have a smaller $^4T_1 \rightarrow {}^6A_1$ transition energy compared to that of Mn^{2+} with mixed PhS^-/S^{2-} coordination (see Figure S7).

Mn^{2+} Stability. Figure 5a shows the gated PL of a N_2-purged acetonitrile solution of Mn:Cd_{10}-2 collected after 2 h

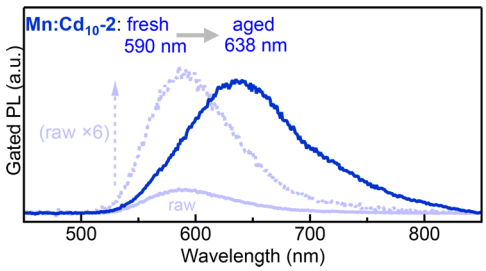

Figure 5. Gated PL spectra of a Mn:Cd_{10}-2 solution collected within 5 min of dissolving in N_2-purged acetonitrile (fresh, light blue) and again after aging for 2 h (aged, dark blue). The intensity of the fresh PL spectrum is ∼6 weaker compared to the aged PL spectrum (dotted, light blue).

(aged Mn:Cd_{10}-2). Initially, the fresh Mn:Cd_{10}-2 solution exhibits Mn^{2+} PL at 590 nm; however, the gated PL spectrum of the aged Mn:Cd_{10}-2 solution shows the peak position redshifts to 638 nm and increases drastically in intensity. No further changes in the peak position were observed at longer times. The gated PL spectrum of Mn:Cd_{10}-1 shows no energy shifts over the same timespan but does exhibit a significant increase in PL intensity (see Figure S10). We attribute this increase in PL intensity from surface Mn^{2+} ions in the aged samples to the longer equilibrium times associated with slow metal-ion exchange kinetics of Cd_{10} (and surface-doped Mn:Cd_{10}). We note that we previously observed relatively slower exchange kinetics for Co^{2+} ions with preformed Cd_{10} compared to preformed Cd_4.[37]

Furthermore, the ESI mass spectrum of aged Mn:Cd_{10}-2 is drastically different from fresh Mn:Cd_{10}-2 and displays similar trends to Mn:Cd_{10}-1 (see Figure 3 and Supporting Information for the full ESI mass spectrum). The spectra of the fresh and aged Mn:Cd_{10}-2 cluster in the same regions from the fragmentation analysis are shown in Figure 6. The relative peak intensity of $[Cd_9MnS_4(SPh)_{14}]^{2-}$ decreases from >60 to 26% after being dissolved in CH_3CN for 2 h. The trend of decreasing relative peak intensity with increasing fragmentation also behaves similar to the results shown in Figure 3 for

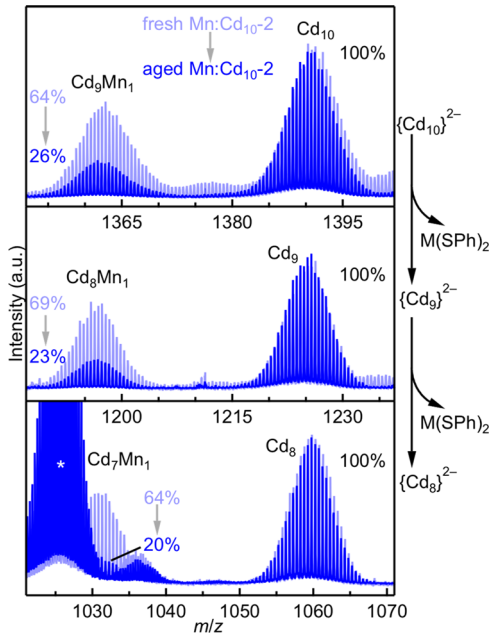

Figure 6. Negative-ion mode ESI mass spectra of Mn:Cd_{10}-2 sample collected immediately after dispersing in N_2-purged CH_3CN (fresh, light blue) and after 2 h (aged, dark blue). The solution was dispersed in N_2-purged CH_3CN (see Supporting Information for full spectrum). The asterisk at *m*/*z* 1024 is $(NMe_4)[Cd_{10}S_4(SPh)_{16}]^{3-}$ ($\delta m/z$ = 0.33).

Mn:Cd_{10}-1. After 2 h, the relative peak intensities of the doped fragments decrease by ∼3% for every $M(SPh)_2$ removed. These combined results are consistent with the majority of Mn^{2+} ions initially located at core site in the Cd_{10} lattice, but over time they have either exchanged with surface Cd^{2+} ions or been removed from the cluster. Thus, the instability of Mn^{2+} in the Cd_{10} core suggests that the core substitution is the kinetic product and hard−soft acid−base arguments still dominate the thermodynamic product with Cd-only cores in the Cd_{10} clusters. Kinetic studies are currently underway to resolve the potential mechanisms responsible for the loss of core dopants in these clusters such as dopant ejection vs dopant exchange from the core to surface sites.

CONCLUSIONS

We presented a synthetic strategy to control the speciation of defects in a small CdS-based molecular cluster. The initial cluster assembly and cluster-to-cluster conversion process were systematically studied and suggest a complex equilibrium exists between Cd_4, Cd_8, and Cd_{10} clusters that all have unique kinetics for metal-ion exchange and ligand interconversion. Through ESI-MS, we observe Mn^{2+}-doped Cd_8, which appears to correlate with the successful incorporation of Mn^{2+} ions at the inner core sites of Cd_{10}. Metal ion exchange only at surface sites is also confirmed when Mn^{2+} is simply added to preformed Cd_{10}.

The combination of negative-ion mode ESI-MS and gated PL spectroscopy allow for unambiguous determination of dopant speciation in Cd_{10}. Specific assignment of dopant locale is supported by the energy of the Mn^{2+}-centered PL that is consistent with variation in average ligand field strengths for the different coordination environments of surface and core metal sites of Cd_{10}. These approaches provide evidence that solution dynamics cannot be overlooked when designing

DOI: 10.1021/acs.chemmater.8b01482
Chem. Mater. 2018, 30, 4720−4727

doped molecular clusters. Future work will encompass exploration of various synthetic routes for doping larger molecular clusters such as Cd_{17}, Cd_{20}, and Cd_{32}, where targeted dopant ions may be efficiently stabilized at core sites due to the larger lattice stabilization energies compared to the smaller Cd_{10}.

■ ASSOCIATED CONTENT

Supporting Information

The Supporting Information is available free of charge on the ACS Publications website at DOI: 10.1021/acs.chemmater.8b01482.

Additional ESI mass spectra and tables, inductively coupled plasma optical emission spectrometry data, absorption spectra, and PL spectra (PDF)

■ AUTHOR INFORMATION

Corresponding Author

*E-mail: kittilstved@chem.umass.edu.

ORCID

Kevin R. Kittilstved: 0000-0002-9852-7454

Notes

The authors declare no competing financial interest.

■ ACKNOWLEDGMENTS

This work was supported by the National Science Foundation (Grant CHE-1454930). Mass spectra were obtained at the University of Massachusetts Mass Spectrometry Center.

■ ABBREVIATIONS

Cd_4, $[Cd_4(SPh)_{10}]^{2-}$; Cd_8, $[Cd_8S(SPh)_{16}]^{2-}$; Cd_{10}, $[Cd_{10}S_4(SPh)_{16}]^{4-}$; Mn:$Cd_{10}$, Mn^{2+}-doped Cd_{10}; ESI-MS, electrospray ionization mass spectrometry; PL, photoluminescence; PLE, photoluminescence excitation; MLCT, metal-to-ligand charge transfer; HOMO, highest-occupied molecular orbital; LUMO, lowest-unoccupied molecular orbital

■ REFERENCES

(1) Beecher, A. N.; Yang, X.; Palmer, J. H.; LaGrassa, A. L.; Juhas, P.; Billinge, S. J.; Owen, J. S. Atomic structures and gram scale synthesis of three tetrahedral quantum dots. *J. Am. Chem. Soc.* **2014**, *136*, 10645−10653.

(2) Gary, D. C.; Flowers, S. E.; Kaminsky, W.; Petrone, A.; Li, X.; Cossairt, B. M. Single-Crystal and Electronic Structure of a 1.3 nm Indium Phosphide Nanocluster. *J. Am. Chem. Soc.* **2016**, *138*, 1510−1513.

(3) Alivisatos, A. P. Semiconductor Clusters, Nanocrystals, and Quantum Dots. *Science* **1996**, *271*, 933−937.

(4) Corrigan, J. F.; Fuhr, O.; Fenske, D. Metal Chalcogenide Clusters on the Border between Molecules and Materials. *Adv. Mater.* **2009**, *21*, 1867−1871.

(5) Farneth, W. E.; Herron, N.; Wang, Y. Bulk Semiconductors from Molecular Solids: A Mechanistic Investigation. *Chem. Mater.* **1992**, *4*, 916−922.

(6) Cumberland, S. L.; Hanif, K. M.; Javier, A.; Khitrov, G. A.; Strouse, G. F.; Woessner, S. M.; Yun, C. S. Inorganic Clusters as Single-Source Precursors for Preparation of CdSe, ZnSe, and CdSe/ZnS Nanomaterials. *Chem. Mater.* **2002**, *14*, 1576−1584.

(7) Fregnaux, M.; Arl, D.; Dalmasso, S. p.; Gaumet, J.-J.; Laurenti, J.-P. Physical and Chemical Analyses on Single-Source Precursor-Grown CdS Semiconductor Nanomaterials. *J. Phys. Chem. C* **2010**, *114*, 17318−17323.

(8) Khitrov, G. A.; Strouse, G. F. ZnS nanomaterial characterization by MALDI-TOF mass spectrometry. *J. Am. Chem. Soc.* **2003**, *125*, 10465−10469.

(9) Tuerk, T.; Resch, U.; Fox, M. A.; Vogler, A. Cadmium benzenethiolate clusters of various size: molecular models for metal chalcogenide semiconductors. *J. Phys. Chem.* **1992**, *96*, 3818−3822.

(10) Nosaka, Y.; Shigeno, H.; Ikeuchi, T. Formation steps of CdS clusters in aqueous solution containing 2-mercaptoethanol. *Surf. Rev. Lett.* **1996**, *03*, 1209−1213.

(11) Eichhöfer, A. Thermal Properties of $[M_{10}Se_4(SePh)_{12}(PR_3)_4]$ (M = Zn, Cd, Hg) Cluster Molecules - Synthesis and Structure of $[Cd_{32}Se_{14}(SePh)_{36}(L)_4]$; L = $OPPh_3$, OC_4H_8. *Eur. J. Inorg. Chem.* **2005**, *2005*, 1245−1253.

(12) Vossmeyer, T.; Reck, G.; Schulz, B.; Katsikas, L.; Weller, H. Double-Layer Superlattice Structure Built Up of $Cd_{32}S_{14}(SCH_2CH(OH)CH_3)_{36}\cdot 4H_2O$ Clusters. *J. Am. Chem. Soc.* **1995**, *117*, 12881−12882.

(13) Eichhöfer, A.; Aharoni, A.; Banin, U. Synthesis, Structure, and Optical Properties of New Cadmium Chalcogenide Clusters of the Type $[Cd_{10}E_4(E'Ph)_{12}(PR_3)_4]$, (E, E′ = Te, Se, S). *Z. Anorg. Allg. Chem.* **2002**, *628*, 2415−2421.

(14) Degroot, M. W.; Taylor, N. J.; Corrigan, J. F. Controlled synthesis of ternary II-II′-VI nanoclusters and the effects of metal ion distribution on their spectral properties. *Inorg. Chem.* **2005**, *44*, 5447−5458.

(15) Zheng, N.; Bu, X.; Lu, H.; Zhang, Q.; Feng, P. Crystalline superlattices from single-sized quantum dots. *J. Am. Chem. Soc.* **2005**, *127*, 11963−11965.

(16) Levchenko, T. I.; Kubel, C.; Khalili Najafabadi, B.; Boyle, P. D.; Cadogan, C.; Goncharova, L. V.; Garreau, A.; Lagugne-Labarthet, F.; Huang, Y.; Corrigan, J. F. Luminescent CdSe Superstructures: A Nanocluster Superlattice and a Nanoporous Crystal. *J. Am. Chem. Soc.* **2017**, *139*, 1129−1144.

(17) Stein, J. L.; Steimle, M. I.; Terban, M. W.; Petrone, A.; Billinge, S. J. L.; Li, X.; Cossairt, B. M. Cation Exchange Induced Transformation of InP Magic-Sized Clusters. *Chem. Mater.* **2017**, *29*, 7984−7992.

(18) Jawaid, A. M.; Chattopadhyay, S.; Wink, D. J.; Page, L. E.; Snee, P. T. Cluster-seeded synthesis of doped CdSe:Cu_4 quantum dots. *ACS Nano* **2013**, *7*, 3190−3197.

(19) Archer, P. I.; Santangelo, S. A.; Gamelin, D. R. Inorganic cluster syntheses of TM^{2+}-doped quantum dots (CdSe, CdS, CdSe/CdS): physical property dependence on dopant locale. *J. Am. Chem. Soc.* **2007**, *129*, 9808−9818.

(20) Fainblat, R.; Barrows, C. J.; Gamelin, D. R. Single Magnetic Impurities in Colloidal Quantum Dots and Magic-Size Clusters. *Chem. Mater.* **2017**, *29*, 8023−8036.

(21) Wu, T.; Zhang, Q.; Hou, Y.; Wang, L.; Mao, C.; Zheng, S. T.; Bu, X.; Feng, P. Monocopper doping in Cd-In-S supertetrahedral nanocluster via two-step strategy and enhanced photoelectric response. *J. Am. Chem. Soc.* **2013**, *135*, 10250−10253.

(22) Lin, J.; Zhang, Q.; Wang, L.; Liu, X.; Yan, W.; Wu, T.; Bu, X.; Feng, P. Atomically precise doping of monomanganese ion into coreless supertetrahedral chalcogenide nanocluster inducing unusual red shift in Mn^{2+} emission. *J. Am. Chem. Soc.* **2014**, *136*, 4769−4779.

(23) Eichhöfer, A.; Hampe, O.; Lebedkin, S.; Weigend, F. Bistrimethylsilylamide transition-metal complexes as starting reagents in the synthesis of ternary Cd-Mn-Se cluster complexes. *Inorg. Chem.* **2010**, *49*, 7331−7339.

(24) Eilers, J.; Groeneveld, E.; de Mello Donega, C.; Meijerink, A. Optical Properties of Mn-Doped ZnTe Magic Size Nanocrystals. *J. Phys. Chem. Lett.* **2012**, *3*, 1663−1667.

(25) Yang, J.; Fainblat, R.; Kwon, S. G.; Muckel, F.; Yu, J. H.; Terlinden, H.; Kim, B. H.; Iavarone, D.; Choi, M. K.; Kim, I. Y.; Park, I.; Hong, H. K.; Lee, J.; Son, J. S.; Lee, Z.; Kang, K.; Hwang, S. J.; Bacher, G.; Hyeon, T. Route to the Smallest Doped Semiconductor: Mn^{2+}-Doped $(CdSe)_{13}$ Clusters. *J. Am. Chem. Soc.* **2015**, *137*, 12776−12779.

DOI: 10.1021/acs.chemmater.8b01482
Chem. Mater. 2018, 30, 4720−4727

(26) Yang, J.; Muckel, F.; Baek, W.; Fainblat, R.; Chang, H.; Bacher, G.; Hyeon, T. Chemical Synthesis, Doping, and Transformation of Magic-Sized Semiconductor Alloy Nanoclusters. *J. Am. Chem. Soc.* **2017**, *139*, 6761−6770.
(27) Soloviev, V. N.; Eichhöfer, A.; Fenske, D.; Banin, U. Size-Dependent Optical Spectroscopy of a Homologous Series of CdSe Cluster Molecules. *J. Am. Chem. Soc.* **2001**, *123*, 2354−2364.
(28) Gaumet, J. J.; Khitrov, G. A.; Strouse, G. F. Mass Spectrometry Analysis of the 1.5 nm Sphalerite−CdS Core of $[Cd_{32}S_{14}(SC_6H_5)_{36}\cdot DMF_4]$. *Nano Lett.* **2002**, *2*, 375−379.
(29) Lee, G. S. H.; Craig, D. C.; Ma, I.; Scudder, M. L.; Bailey, T. D.; Dance, I. G. $[S_4Cd_{17}(SPh)_{28}]^{2-}$, the 1st Member of a 3rd Series of Tetrahedral $[S_wM_x(SR)_Y]^{Z-}$ Clusters. *J. Am. Chem. Soc.* **1988**, *110*, 4863−4864.
(30) Herron, N.; Suna, A.; Wang, Y. Synthesis of ≈10 Å thiophenolate-capped CdS clusters. Observation of a sharp absorption peak. *J. Chem. Soc., Dalton Trans.* **1992**, 2329−2335.
(31) Levchenko, T. I.; Lucier, B. E. G.; Corrigan, J. F.; Huang, Y. Crystalline Superlattices of Nanoscopic CdS Molecular Clusters: An X-ray Crystallography and ^{111}Cd SSNMR Spectroscopy Study. *Inorg. Chem.* **2018**, *57*, 204−217.
(32) Lee, G. S. H.; Fisher, K. J.; Craig, D. C.; Scudder, M. L.; Dance, I. G. $[ECd_8(E'Ph)_{16}]^{2-}$ cluster chemistry (E, E′ = sulfur, selenium, tellurium). *J. Am. Chem. Soc.* **1990**, *112*, 6435−6437.
(33) Swenson, D.; Baenziger, N. C.; Coucouvanis, D. Tetrahedral mercaptide complexes. Crystal and molecular structures of $[(C_6H_5)_4P]_2M(SC_6H_5)_4$ complexes (M = cadmium(II), zinc(II), nickel(II), cobalt(II), and manganese(II)). *J. Am. Chem. Soc.* **1978**, *100*, 1932−1934.
(34) Bendova, M.; Puchberger, M.; Pabisch, S.; Peterlik, H.; Schubert, U. Studies on the Formation of CdS Nanoparticles from Solutions of $(NMe_4)_4[Cd_{10}S_4(SPh)_{16}]$. *Eur. J. Inorg. Chem.* **2010**, *2010*, 2266−2275.
(35) Dance, I. G.; Choy, A.; Scudder, M. L. Syntheses, Properties, and Molecular and Crystal-Structures of $(Me_4N)_4[E_4M_{10}(SPh)_{16}]$ (E = S, Se; M = Zn, Cd): Molecular Supertetrahedral Fragments of the Cubic Metal Chalcogenide Lattice. *J. Am. Chem. Soc.* **1984**, *106*, 6285−6295.
(36) Pittala, S.; Kittilstved, K. R. Cation exchange in small ZnS and CdS molecular analogues. *Inorg. Chem.* **2015**, *54*, 5757−5767.
(37) Pittala, S.; Mortelliti, M. J.; Kato, F.; Kittilstved, K. R. Substitution of Co^{2+} ions into CdS-based molecular clusters. *Chem. Commun.* **2015**, *51*, 17096−17099.
(38) Hagen, K. S.; Stephan, D. W.; Holm, R. H. Metal ion exchange reactions in cage molecules: the systems $[M_{4-n}M'_n(SC_6H_5)_{10}]^{2-}$ (M, M′ = Fe(II), Co(II), Zn(II), Cd(II)) with adamantane-like stereochemistry and the structure of $[Fe_4(SC_6H_5)_{10}]^{2-}$. *Inorg. Chem.* **1982**, *21*, 3928−3936.
(39) Løver, T.; Henderson, W.; Bowmaker, G. A.; Seakins, J. M.; Cooney, R. P. Electrospray Mass Spectrometry of Thiophenolate-Capped Clusters of CdS, CdSe, and ZnS and of Cadmium and Zinc Thiophenolate Complexes: Observation of Fragmentation and Metal, Chalcogenide, and Ligand Exchange Processes. *Inorg. Chem.* **1997**, *36*, 3711−3723.
(40) Comeau, A. N.; Liu, J.; Khadka, C. B.; Corrigan, J. F.; Konermann, L. Nanocluster isotope distributions measured by electrospray time-of-flight mass spectrometry. *Anal. Chem.* **2013**, *85*, 1200−1207.
(41) Gaumet, J. J.; Strouse, G. Nanospray mass spectrometry technique for analysing nanomaterials from molecular precursors up to 1.5 nm in diameter cluster. *Mater. Sci. Eng., C* **2002**, *19*, 299−304.
(42) Arl, D.; Aubriet, F.; Gaumet, J. J. Study by ESI-FTICRMS and ESI-FTICRMS(n) of zinc and cadmium thiophenolate complexes used as precursors for the synthesis of II-VI nanosemiconductors. *J. Mass Spectrom.* **2009**, *44*, 763−771.
(43) Gaumet, J.-J.; Strouse, G. Mass Spectrometry Analysis of Organic-Inorganic Nanomaterials and their Precursors. *MRS Online Proc. Libr.* **2002**, *726*, Q10.6.
(44) Gaumet, J.-J.; Strouse, G. F. Electrospray mass spectrometry of semiconductor nanoclusters: comparative analysis of positive and negative ion mode. *J. Am. Soc. Mass Spectrom.* **2000**, *11*, 338−344.
(45) Desireddy, A.; Conn, B. E.; Guo, J.; Yoon, B.; Barnett, R. N.; Monahan, B. M.; Kirschbaum, K.; Griffith, W. P.; Whetten, R. L.; Landman, U.; Bigioni, T. P. Ultrastable silver nanoparticles. *Nature* **2013**, *501*, 399−402.
(46) Negishi, Y.; Nobusada, K.; Tsukuda, T. Glutathione-protected gold clusters revisited: bridging the gap between gold(I)-thiolate complexes and thiolate-protected gold nanocrystals. *J. Am. Chem. Soc.* **2005**, *127*, 5261−5270.
(47) Negishi, Y.; Munakata, K.; Ohgake, W.; Nobusada, K. Effect of Copper Doping on Electronic Structure, Geometric Structure, and Stability of Thiolate-Protected Au_{25} Nanoclusters. *J. Phys. Chem. Lett.* **2012**, *3*, 2209−2214.
(48) Strohalm, M.; Kavan, D.; Novak, P.; Volny, M.; Havlicek, V. mMass 3: a cross-platform software environment for precise analysis of mass spectrometric data. *Anal. Chem.* **2010**, *82*, 4648−4651.
(49) Mattapalli, H.; Monteith, W. B.; Burns, C. S.; Danell, A. S. Zinc deposition during ESI-MS analysis of peptide-zinc complexes. *J. Am. Soc. Mass Spectrom.* **2009**, *20*, 2199−205.
(50) Autissier, V.; Henderson, R. A. Mechanism of Single Metal Exchange in the Reactions of $[M_4(SPh)_{10}]^{2-}$ (M = Zn or Fe) with CoX_2 (X = Cl or NO_3) or $FeCl_2$. *Inorg. Chem.* **2008**, *47*, 6393−6403.
(51) van Driel, A. F.; Nikolaev, I. S.; Vergeer, P.; Lodahl, P.; Vanmaekelbergh, D.; Vos, W. L. Statistical analysis of time-resolved emission from ensembles of semiconductor quantum dots: Interpretation of exponential decay models. *Phys. Rev. B: Condens. Matter Mater. Phys.* **2007**, *75*, 035329.
(52) Nag, A.; Cherian, R.; Mahadevan, P.; Gopal, A. V.; Hazarika, A.; Mohan, A.; Vengurlekar, A. S.; Sarma, D. D. Size-Dependent Tuning of Mn^{2+} d Emission in Mn^{2+}-Doped CdS Nanocrystals: Bulk vs Surface. *J. Phys. Chem. C* **2010**, *114*, 18323−18329.
(53) Nguyen, K. A.; Pachter, R.; Day, P. N.; Su, H. Theoretical analysis of structures and electronic spectra in molecular cadmium chalcogenide clusters. *J. Chem. Phys.* **2015**, *142*, 234305.
(54) Tanabe, Y.; Sugano, S. On the Absorption Spectra of Complex Ions. I. *J. Phys. Soc. Jpn.* **1954**, *9*, 753−766.
(55) Holah, D. G.; Coucouvanis, D. Synthesis and characterization of a new series of first row element tetrahedral mercaptide complexes. *J. Am. Chem. Soc.* **1975**, *97*, 6917−6919.
(56) Nakata, M.; Ueyama, N.; Nakamura, A.; Nozawa, T.; Hatano, M. Circular dichroism and magnetic circular dichroism spectra of tetrahedral cobalt(II) complexes of thiophenolate, *o*-xylene-α,α′-dithiolate, and L-cysteine-containing oligopeptides. *Inorg. Chem.* **1983**, *22*, 3028−3035.
(57) Pappalardo, R.; Dietz, R. E. Absorption Spectra of Transition Ions in CdS Crystals. *Phys. Rev.* **1961**, *123*, 1188−1203.
(58) Brorson, M.; Schaeffer, C. E. Orthonormal Interelectronic Repulsion Operators in the Parametrical d^q Model. Application of the Model to Gaseous Ions. *Inorg. Chem.* **1988**, *27*, 2522−2530.

DOI: 10.1021/acs.chemmater.8b01482
Chem. Mater. 2018, 30, 4720−4727